




On the origin of the Hercules group: II. the Trojan quasi-periodic identity on the orbital level

Yusen Li (李宇森)¹  ^{*} Kenneth Freeman¹  [†] Helmut Jerjen¹ 

¹Research School of Astronomy and Astrophysics, Australian National University, Canberra, ACT 2611, Australia

Accepted XXX. Received YYY; in original form ZZZ

ABSTRACT

The Hercules structure is a stellar kinematic group anomaly observed in the solar neighbourhood (SNd). In the previous paper, we analysed chemical signatures and related the origin of this stellar population to the outer bar. Next to consider is how this alien population migrate out into the SNd. Often, the formation of this kinematic structure is associated with bar resonances. In this paper, We consider the driving mechanism of Hercules on the orbital level. We construct a simple Milky Way-like potential model with a slowly rotating long bar and explore some of the stellar orbit families and their stability. With this model, our numerical solutions of the equations of motion show that extended quasi-periodic orbits trapped around fast-rotating periodic orbits around the L4 Lagrange point of the bar minor axis can pass through the SNd. When observed in the SNd, they populate the Hercules structure in the L_Z - V_R kinematics space. Moreover, the variation in radial coverage in the galactic plane with the SNd kinematics shows good agreement with chemical signatures found in Paper I. Furthermore, the effective potential shows the topology of a volcano, the rim of which limits most orbits to stay inside or outside. Trojan orbits are a stable orbit family that can transport inner Galactic stars out to the SNd. They can explain the stellar kinematics of the Hercules group, and provide a straightforward basis for its chemical properties (see Paper I). We support the view that Trojan orbits associated with the slowly rotating Galactic bar explain the Hercules structure observed in SNd.

Key words: Galaxy: kinematics and dynamics – Galaxy: solar neighbourhood – galaxies: bar

1 INTRODUCTION

The distribution of stars in the solar neighbourhood (the SNd) reveals many structures in the Galactocentric cylindrical angular momentum - radial velocity (L_Z - V_R) plane as overdensities, as shown in Fig. 1. These structures are often referred to as *kinematic groups*. Historically, due to different assumptions on the underlying mechanism, these kinematic groups have been referred to as “*moving groups*” (Eggen 1983, 1996) and “*dynamical streams*” (Famaey et al. 2005).

Among the kinematic groups, one of the most extensively studied groups is the Hercules group, marked by the cyan dashed contour. The Hercules group shows an asymmetry skewed toward outward radial velocity and includes angular momentum, $L_Z \sim 1300$ to 1700 kpc km s⁻¹, well below the Local Standard of Rest (LSR), $L_Z \sim 1900$ kpc km s⁻¹. Chemical data have identified the Hercules group as a distinctly Fe-enhanced structure in the SNd (e.g. Bensby et al. 2007; Quillen et al. 2018; Khoperskov & Gerhard 2022). As the metallicity of the local interstellar medium (ISM) is near-solar to subsolar (e.g. Pagel & Edmunds 1981; Asplund et al. 2009), these chemical signatures suggest an origin of the Hercules stars from outside the SNd. Our previous paper (Li, Freeman, & Jerjen 2024; hereafter Paper I) investigated chemical and age features with data from GALAH DR4 (Buder et al. 2024) and APOGEE DR17 (Abdurro’uf et al. 2022). We found an iron-peak-enhanced,

alpha-deficient, and odd-Z-enhanced population in the low L_Z Hercules subgroups III and IV. This population is expected to originate from the outer thin bar and migrate to the SNd via some dynamical mechanism.

Due to the asymmetry in V_R , early studies associated the Hercules group with the Outer Lindblad Resonance (OLR) of the non-axisymmetric central Galactic bar (Kalnajs 1991; Dehnen 2000). This scenario is well supported by a fast rotating short bar with pattern speed $\Omega_b \sim 56$ km s⁻¹ kpc⁻¹ (Antoja et al. 2014; Monari et al. 2017). However, recent photometric and spectroscopic surveys of the structure of the inner Galaxy (Wegg et al. 2015; Portail et al. 2017) suggest a different model with a longer bar that rotates slower. The new model has a bar semi-major length $a \sim 5$ kpc and a pattern speed $\Omega_b \sim 39$ km s⁻¹ kpc⁻¹. The new model places the OLR at $R \sim 10.5$ kpc, more than 2 kpc outside the orbit of the sun, $R_\odot \sim 8.2$ kpc (GRAVITY Collaboration et al. 2019, 2021). Hence the OLR scenario is less favoured as the Hercules origin.

Recent studies explain the origin of the Hercules group differently. Hunt & Bovy (2018) and Asano et al. (2020) explained Hercules as the 4:1 OLR of the bar. Hunt et al. (2018), Michtchenko et al. (2018), and Barros et al. (2020) explored a possible origin related to the Inner Lindblad Resonances of the spirals. Khoperskov & Gerhard (2022) and Liang et al. (2023) proposed a complex scenario where the spiral arm and bar resonances both contribute to the Hercules structure and substructures. Other works attributed the Hercules structures to the corotation resonance of the long bar (e.g. Monari et al. 2019; Binney 2020; Wheeler et al. 2022; and Lucchini et al. 2024). Among

* E-mail: li.yusen.astr@gmail.com

† E-mail: kenneth.freeman@anu.edu.au

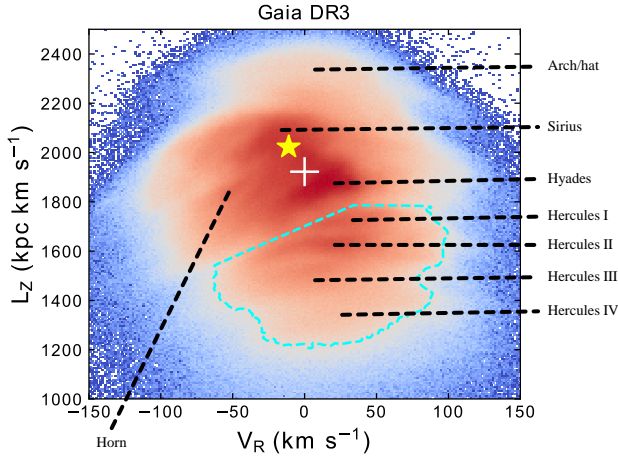


Figure 1. The distribution of more than 8 M the SNd stars in *Gaia* DR3 in the planar angular momentum-radial velocity plane. The yellow asterisk and the white cross mark the solar and the LSR kinematics. The Hercules structure, subdivided into four subgroups, is marked by the dashed cyan contour. We associate eight over-densities as kinematic groups.

works supporting the corotation theory, Pérez-Villegas et al. (2017) and D’Onghia & L. Aguerrí (2020) examined the mechanism in finer detail, from the perspective of stellar orbits. They propose orbits around the L4 and L5 Lagrange points on the bar minor axis as building blocks of the Hercules structure. These orbits are often referred to as Trojan orbits, analogous to the orbits of planetary Trojan asteroid families, which are also trapped around the L4 and L5 Lagrange points in the stellar-planar restricted three-body problem (Murray & Dermott 1999). However, most of the previous studies were based on N-body simulations. While simulations provide self-consistent Galaxy models, we investigate the Trojan orbit scenario at the stellar orbital level and relate the dynamical theory to footprints in chemical abundances in this paper.

We adopt a simple but realistic barred potential model and restrict our scope to motions in the galactic plane to capture some general properties of regular planar orbits in barred disc galaxies. In the next paper, we plan to adopt a more realistic, observation-based, 3D potential of the Milky Way Galaxy that includes details of the inner Galaxy with a boxy peanut-shaped bulge and a super thin long bar (Sormani et al. 2022; Hunter et al. 2024). We will use this more realistic model to consider possible inner galactic orbits that might be captured by the Trojan orbits and the origins of the super thin bar with a vertical scale height only about ~ 40 pc (Wegg et al. 2015).

In § 2, we present the analytical model of the barred galaxy potential to study the orbital dynamics. In § 3, we investigate the nature of Trojan orbits with the gravitational model as quasi-periodic orbits around stable periodic orbit families around the stable L4 Lagrange point, and analyse the behaviours and stability of these orbits with their surfaces of section. In § 4, we relate orbital studies with chemical signatures found in Paper I and discuss possible scenarios of capturing inner Galactic stars into Trojan orbits. A summary is given in § 5.

2 DATA AND MODEL

2.1 Data

We follow the methods presented in our previous paper to obtain the kinematics data from *Gaia* DR3 (Gaia Collaboration et al. 2023). We obtain the 6D phase space kinematics of proper motions, line-of-sight radial velocity, and parallax in *Gaia*. By assuming a Local Standard of Rest (LSR) with a tangential velocity of $v_{T, \text{LSR}} = 235 \text{ km s}^{-1}$, they are then transformed into Galactocentric cylindrical coordinates with angular momentum $L_Z = V_T R$ and radial velocity V_R , positive away from the Galactic centre. The solar neighbourhood (the SNd) is defined as a cylinder with radius $R_{\text{the SNd}} = 1 \text{ kpc}$ and height $Z_{\text{the SNd}} = 1 \text{ kpc}$ centred radially and vertically at the sun.

The resulting distribution in the L_Z - V_R plane, as presented in Fig. 1, shows the 8 most prominent kinematic groups. We observe the high L_Z Arch/Hat; the slightly negative V_R -biased Sirius; the most populated Hyades; the Horn on the left of Hyades; and the 4 Hercules subgroups. The LSR and solar kinematics are marked by the white cross and the yellow asterisk for reference. The Hercules group includes about 23 per cent of stars in the SNd under our definition. This fraction varies slightly among the surveys used (*Gaia*, GALAH, APOGEE).

2.2 The simple dynamical model

As the Hercules stars are defined by the pattern in the kinematics plane, we wish to understand their dynamical features. To study the stellar orbits in the Galaxy, we construct a barred analytic gravitational potential that models the Galaxy. Our barred model include our current best understanding of the Galactic bar as a long, slowly rotating bar. However, we note that different bar parameters (e.g. a faster bar) would result in models that support different results and conclusions. As an example, a scenario associated with the outer Lindblad resonance (OLR) is favoured for the formation of Hercules in a short, fast bar model (e.g. Dehnen 2000; Antoja et al. 2014).

We set our frame of reference corotating with the galactic bar, and align the x-axis with the bar major axis. We let the bar rotate clockwise as seen in Fig. 2, consistent with our presentation of the *Gaia* kinematic data. We adopt a thin-disc plus dark halo approximation of the Galaxy and restrict our study to the 2-dimensional Galactic plane to study regular planar stellar motions.

In this model, the conservation of angular momentum (L_Z) and energy (E) does not hold in general. Instead, the Hamiltonian (or the Jacobi Integral E_J) in the rotating frame, is the only conserved quantity that can be written in analytic form.

$$E_J = \frac{1}{2} |\dot{\mathbf{r}}|^2 + \Phi_{\text{eff}} = E - \Omega_b L_Z, \quad (1)$$

where $\Phi_{\text{eff}} = \Phi - \frac{1}{2} \Omega_b^2 |\mathbf{r}|^2$ is the effective potential in the frame corotating with the bar, which has angular velocity Ω_b , and \mathbf{r} & $\dot{\mathbf{r}}$ are the planar position and velocity. In general, analytical solutions for orbits in such rotating potentials are rare (e.g. Freeman 1966). Hence, we rely on numerical solutions for most of the understanding on orbital properties in this barred galaxy model.

For this purpose, an analytical non-axisymmetric bar potential Φ_b is combined with an axisymmetric component Φ_d that accounts for the distribution from the bulge, disc, and dark halo of the galaxy to simulate the flat rotation curve widely observed in many disc galaxies including the Milky Way (Eilers et al. 2019).

In this rotating frame, the equations of stellar motion are,

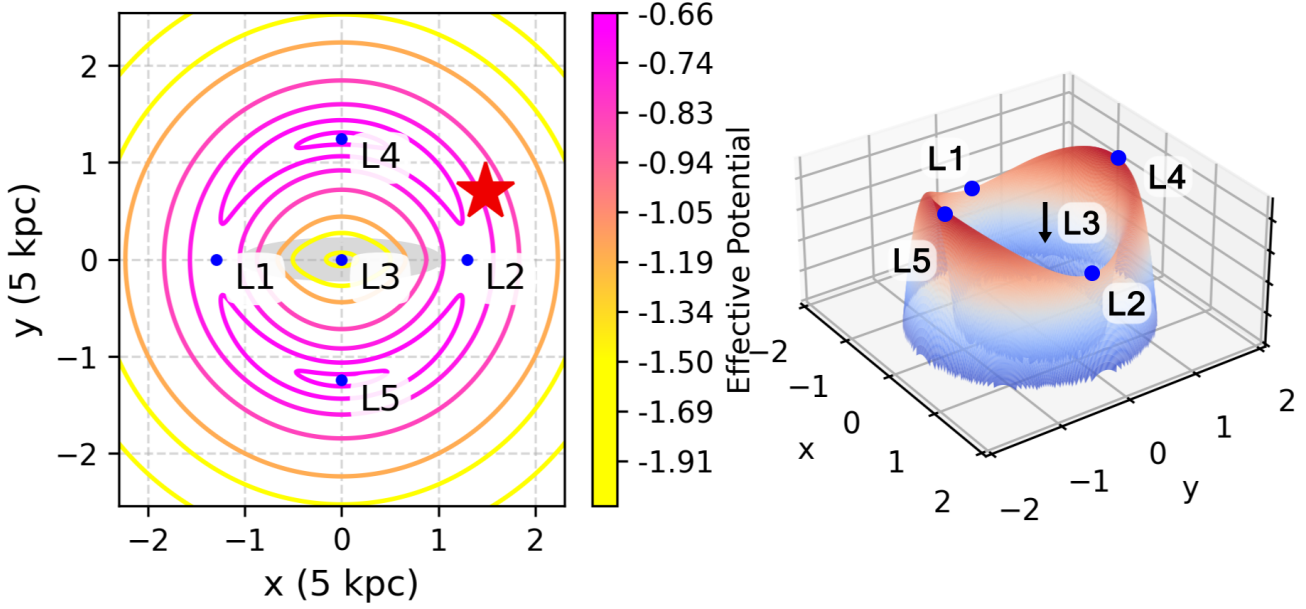


Figure 2. The effective gravitational potential of the combined model. Left: contour plot of the combined potential. The five critical points (Lagrange points) are marked by blue points. The position of the sun is marked by the red star. Right: 3D plot of the volcano-like topology of the effective potential.

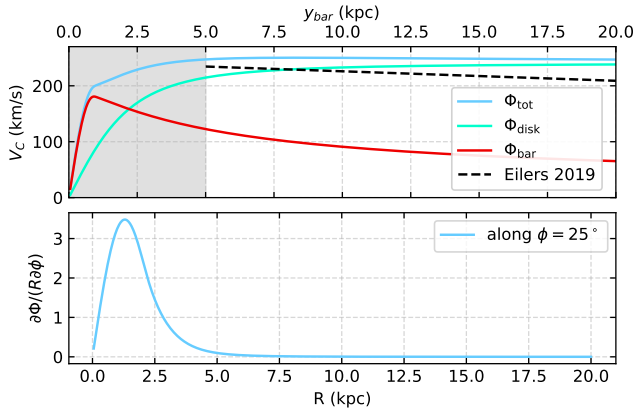


Figure 3. Rotation curve and azimuthal force induced by the potential model. Top: the rotation curve generated by the different components in the model along the y -axis. The observational fitted rotation curve from Eilers et al. (2019) is plotted for comparison; Bottom: the azimuthal force along the sun at different galactic radii in the model.

$$\ddot{x} = -2\Omega_b \dot{y} + \frac{\partial \Phi}{\partial x} + \Omega_b^2 x, \quad (2)$$

$$\ddot{y} = 2\Omega_b \dot{x} + \frac{\partial \Phi}{\partial y} + \Omega_b^2 y, \quad (3)$$

where x and y are Cartesian coordinates in the rotating frame, $\Omega_b = 40 \text{ km s}^{-1} \text{ kpc}^{-1}$ is the pattern speed of the galactic bar, and Φ is the total potential with two components $\Phi = \Phi_b + \Phi_d$.

For the potential induced by the Galactic bar, the main contributor to non-axisymmetry, we adopt the Ferrers bar potential (Ferrers 1877; Perek 1962; de Vaucouleurs & Freeman 1972). The Ferrers bar is an inhomogeneous spheroidal bar with a density distribution $\rho = \rho_0(1 - m^2)^2$, where $m^2 = x^2/a^2 + (y^2 + z^2)/c^2$. In this form, $c < a$

are the semi-major and semi-minor axis of the bar. The potential induced by such a bar is given by,

$$\Phi_b = \frac{105GM_b}{32\epsilon} \tilde{\phi}_b,$$

where $\epsilon^2 = a^2 - c^2 = (5 \text{ kpc})^2$ is a scale length determined by the semi-major (a) and semi-minor (c) axes of the bar, $M_b = 2 \times 10^{10} M_\odot$ is the mass of the bar, and $\tilde{\phi}_b$ can be obtained by recurrence relations. The expression of the potential can be found in closed form in de Vaucouleurs & Freeman (1972) and Appendix A. This model has been used by many studies regarding orbit families in barred galaxies (Athanasoula 1992; Binney & Tremaine 2008; Kim et al. 2012). The Ferrers bar potential represents the potential induced by a prolate spheroid with parameters with physical meanings. Hence it is an idealised simple model of the bar but is sufficiently complicated to capture observational properties of the bar (e.g. the updated semi-major length $a \sim 5 \text{ kpc}$).

For the axisymmetric component, a simple 2D logarithmic potential is adopted to mimic a flat galactic rotation curve,

$$\Phi_d = -\frac{1}{2}V^2 \ln(r^2 + R_c^2),$$

where $r^2 = x^2 + y^2$ is the radius away from the galactic centre. In this potential, V represents the flat galaxy rotation curve in the galactic plane, and R_c is a constant that controls the shape of the rotation curve in the inner Galaxy $R \ll R_c$. Parameters $V = 240 \text{ km s}^{-1}$ and $R_c = 2.5 \text{ kpc}$ are chosen to mimic the flat rotation curve found in many disc galaxies including the Milky Way (Eilers et al. 2019).

We make this system dimensionless by normalising length and time. The lengths are normalised by the scale length, $r = \tilde{r}\epsilon = \tilde{r} \cdot (5 \text{ kpc})$, where \tilde{r} is the length in the system and r represents the lengths in space with physical units. The times are normalised by the bar angular frequency, $t = \tilde{t}/\Omega_b = \tilde{t}/(40 \text{ km s}^{-1} \text{ kpc}^{-1})$, where \tilde{t} is the time in the system, and t represents the actual time.

Then, by dropping the tildes (writing \tilde{x} as x) and collecting constant terms, we obtain two dimensionless numbers,

$$Q = \frac{105GM_b}{32\Omega_b^2\epsilon^3},$$

$$P = \frac{V^2}{\Omega_b^2\epsilon^2},$$

$$\frac{Q}{P} = 0.98\left(\frac{M_b}{2 \times 10^{10} M_\odot}\right)\left(\frac{\epsilon}{5 \text{ kpc}}\right)^{-1}\left(\frac{V}{240 \text{ km s}^{-1}}\right)^{-2}.$$

With these dimensionless numbers, the equations of motion in the dimensionless system can be written as,

$$\ddot{x} = -2\dot{y} + Q \frac{\partial\Phi_b}{\partial x} - P \frac{x}{r^2 + R_c^2} + x, \quad (4)$$

$$\ddot{y} = 2\dot{x} + Q \frac{\partial\Phi_b}{\partial y} - P \frac{y}{r^2 + R_c^2} + y. \quad (5)$$

The model potential in the rotating frame, the effective potential, is presented in Fig. 2. The left panel shows a contour plot with the bar marked as the grey ellipse in the middle and the sun as the red asterisk. As shown, this barred potential has five stationary points, or Lagrange points, marked from L1 to L5. These points are stationary points in the effective potential where $\nabla\Phi_{\text{eff}} = 0$, and static particles stay at these points in the rotating frame. Among the five points, L1 and L2 are non-stable saddle points, L3 is a stable minimum, and L4 and L5 are maxima, stable in most realistic potentials (Sellwood & Wilkinson 1993) and in our potential. Together, the effective potential shows a topology analogous to a “volcano”, as shown in the right panel of Fig. 2: the maxima L4, L5 and saddles points L1, L2 define the “rim” together and the central minimum L3 sits in the “crater” inside the rim. Under this analogy, the sun is located slightly outside the rim.

The rotation curve along the y -axis, generated by the separate and combined components of this model, is presented in the top panel of Fig. 3. This potential, while simple, is sufficiently complex to capture stable in-plane features of the Milky Way, with a long, slow bar and a flat rotation curve. The non-axisymmetric bar mainly contributes to the potential in the inner galaxy $R < 10$ kpc. Outside 10 kpc, the rotation curve is dominated by the axisymmetric component: the disc and the dark matter halo. Although slightly higher, the combined rotation curve shows a good match to the observed rotation curve of the Milky Way (e.g. Eilers et al. 2019), which is marked by the dashed black line. Note that the innermost galaxy ($R < 5$ kpc) is dominated by the non-axisymmetric bar and is not well understood due to limits in observation and is therefore shaded.

The azimuthal force $\partial\Phi/(R\partial\phi)$ along the 25° line passing our Sun and the Galactic centre is shown in the bottom panel. Since the logarithmic component of the potential is axisymmetric, the azimuthal forces are contributed only by the Ferrers bar. The bar-induced axisymmetry mainly exists in the innermost ~ 6 kpc, and the galactic disc becomes nearly axisymmetric outside 7 kpc.

3 ANALYSIS

To consider the Trojan scenario, we investigate the properties of Trojan orbits with the dynamical model in § 3.1. We then relate Trojan orbits to the kinematics observed in the SNd in § 3.2. Finally, we consider the stability of Trojan orbits with surface of section and look into other related orbit families in the model in § 3.3 and § 3.4.

3.1 Trojan orbits

As a kinematic anomaly, the Hercules group is expected to have a dynamical origin. In this section, we adopt orbital dynamics to look into a popular scenario, in which the Hercules group is associated with the corotation resonance of the long slow bar (Pérez-Villegas et al. 2017; Binney 2020; D’Onghia & L. Aguerri 2020). We intend to understand the Corotation origin at the orbit level and evaluate the likelihood of the Trojan scenario.

Among the five Lagrange points, points on the bar minor axis, L4 and L5 are of primary interest. These points are stable maxima and can trap stars. These stars are called Trojans, and we call their orbits Trojan orbits. As static particles remain static at Lagrange points in the Corotating frame, the non-central Lagrange points are associated with Corotation resonance.

Numerical integrations are conducted to obtain numerical solutions of stellar orbits in the 4D phase space. Thanks to the analytic potential in closed form, the potential gradients are analytically determined, and by setting up an initial condition in the phase space, the orbit can be simulated by numerically integrating the equations of motion (Equations 4 and 5) in the rotating frame in the dimensionless system.

We limit our study to orbits that are symmetric about the y -axis (the bar minor axis). The initial positions of orbits are restricted to the y -axis and the initial velocities are set parallel with the x -axis and to the right ($x_0 = 0, y_0 = 0, \dot{x}_0 > 0$). This leaves y_0 and \dot{x}_0 as initial conditions, and as the direction of \dot{x}_0 is assumed, \dot{x}_0 can be replaced by the conserved quantity E_J . Because we adopt a time-independent potential in the rotating frame, a set of initial conditions determines an orbit. As numerical integrations in our work are well-conditioned, numerical solvers do not introduce further instability. Therefore, each set of (E_J, y_0) determines a specific orbit and we refer to the space of (E_J, y_0) as the initial condition space. In this study, the orbits are integrated for a time interval $\Delta t = 500$, which corresponds to about 12 Gyrs. The snapshots of the phase space (x, y, \dot{x}, \dot{y}) are recorded every 1/200 unit time (100,000 time steps in total). The numerical solutions are validated by the conservation of Jacobi integral E_J . In the study, E_J remains constant to at least 6 significant figures.

Stellar motions in this system are non-linear and orbits can be divided into three categories: *chaotic*, *quasi-periodic*, and *periodic* (Sellwood & Wilkinson 1993; Binney & Tremaine 2008). *Chaotic* orbits only have one integral of motion E_J and they are free to explore a hypervolume in the phase space $(\mathbf{r}, \dot{\mathbf{r}})$. The randomness in these orbits suggests that they are more likely to form backgrounds than stable kinematic patterns. *Periodic* or closed orbits, on the other hand, revisit the initial condition and form closed loops. The periodicity emphasises the importance of these orbits due to their capability of forming and preserving stellar structures. However, the family of periodic orbits is a lower dimensional set in the initial condition space and thus has zero measure or probability. Hence, periodic orbits usually do not directly form structures. *Quasi-periodic* orbits (QPO) oscillate around stable periodic orbits in a sense similar to the epicyclic motion in axisymmetric disc galaxies or stellar systems. Hence, these orbits conserve an integral in addition to E_J and form 2D subsets of the initial condition space. These orbits cover a larger area of the initial condition space and form the backbone of the Trojan theory for the formation of the Hercules group.

In our model, the minor axis Lagrange points L4 and L5 trap two families of periodic orbits, the slow, banana-shaped and the fast, more circular periodic orbits, presented in the bottom panel of Fig. 4. Both families are retrograde, against bar rotation in the rotating frame. In physical units, the orbits in the slow Trojan orbits have frequencies

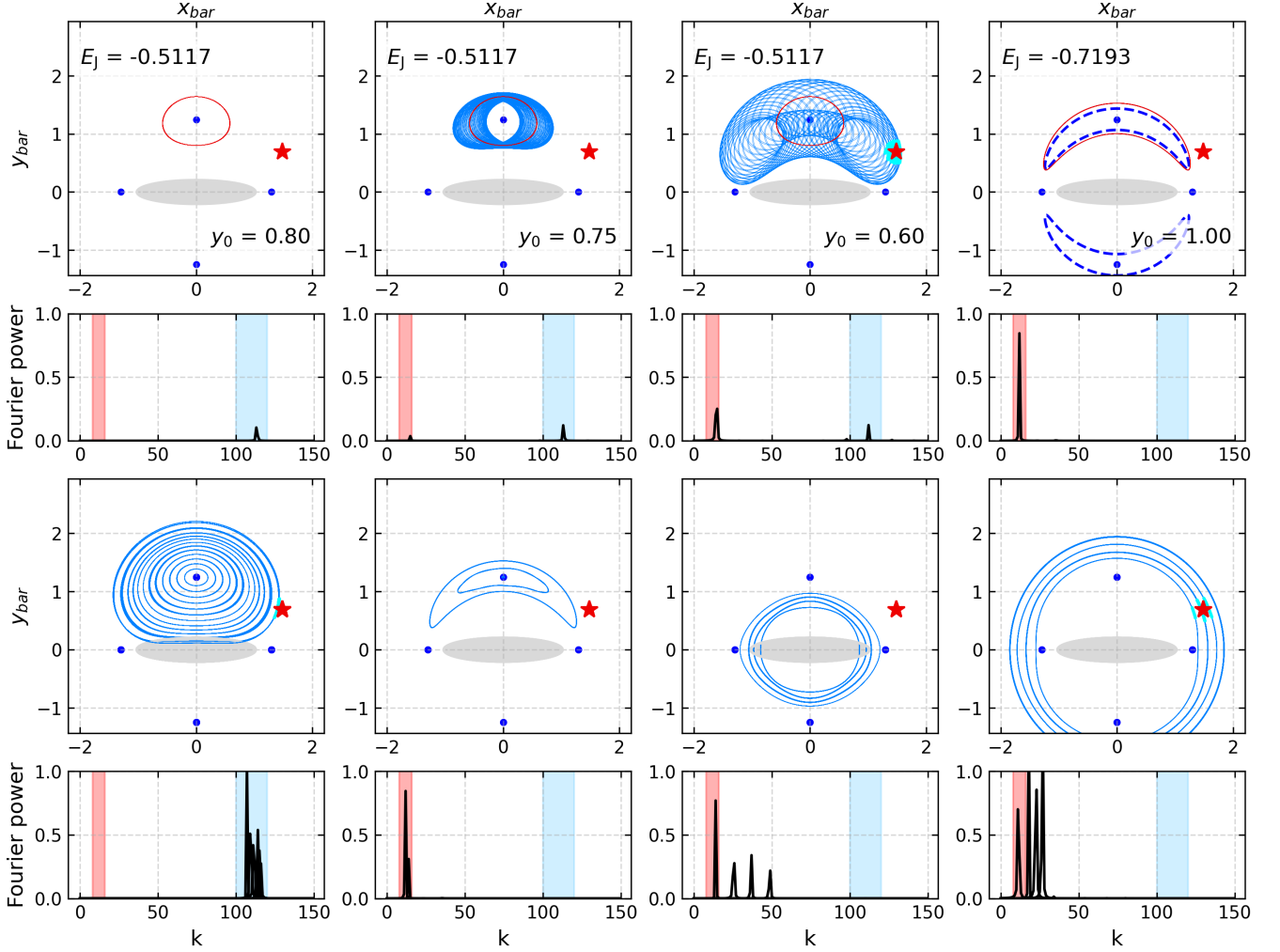


Figure 4. Trojan orbits and their corresponding Fourier power spectrum. The red star marks the sun and the cyan marks the orbit crossing the SNd. Top left: a fast Trojan periodic orbit; Top right: a slow Trojan periodic orbit; Top middle: morphologies of two QPOs perturbed from the fast orbit on Top left; Bottom: four periodic orbit families. The orbits in fast and slow families share similar frequencies to other members of the family. The approximate range of the frequencies is shaded, slow family in red and the fast family in blue.

about $f_s \sim 1 \text{ Gyr}^{-1}$ while the fast Trojan orbits have frequencies about $f_f \sim 9 \text{ Gyr}^{-1}$. The slow orbits wallow through the potential as the Coriolis force balances the potential gradient, while the fast orbits are more energetic, cross through equipotentials, and exhibit much stronger Coriolis force to support the centripetal force required. As the effective potential is symmetric about the x -axis, all orbits on the near side of the galaxy exist centrosymmetrically about the galactic centre on the other side. Hence, although we draw our attention primarily to the L4 orbits, we should note that centrosymmetric families also exist around L5.

These two periodic orbit families are both stable and can form families of quasi-periodic orbits under perturbations. Practically, orbits are determined by E_J and y_0 , and as E_J is an integral that is conserved in an orbit, we achieve perturbations by slightly changing the initial position y_0 while holding E_J constant. The quasi-periodic orbits can be found by perturbing in both directions. The top right plot in Fig. 4 shows a banana-shaped slow orbit, which follows the curves of zero velocity (ZVC). The ZVC occurs where the Jacobi integral of the orbit is below the maximum effective potential, at L4, $E_J < \max(\Phi_{\text{eff}}) = \Phi_{\text{eff}, L4}$. Therefore, from Equation 1, there ex-

ists a region where the kinetic energy in the rotating frame becomes negative, so the region is non-explorable by the orbit. The QPOs of the slow family are more fragile under large perturbation while QPOs of the fast family are very stable, capable of tolerating large perturbations in the initial condition y_0 . This results in very extended QPOs that travel as far as 5 kpc away from the parent orbit.

To better understand these quasi-periodic orbits as epicycles, we conduct spectral stellar dynamics analysis (Binney & Spergel 1982) on the orbits in the Trojan family. We Fourier transform the x -coordinates $x(t)$ of an orbit and plot the Fourier power spectrum against frequency under each orbit plot in Fig. 4. On the top panel, we take a Trojan periodic orbit with $E_J = -0.5117$ and perturb it to show different morphological states of the QPOs. In each plot, the periodic orbits are coloured in red while the QPO perturbed from them is shown in blue. The leftmost orbit shows the parent periodic orbit with no perturbation applied. With very little perturbation, the near-circular orbit “thickens” slightly and largely remains in the original shape. Under larger perturbations, the QPO forms very extended orbits that can reach the SNd. As we will see, these QPOs can form the building blocks of the Hercules structure. By considering

the power spectra of two periodic orbits on the leftmost and rightmost plots in the top panel, we see that the circular fast periodic orbit corresponds to a single high frequency, with wave number $\kappa_f \sim 110$ and the banana-shaped periodic orbit corresponds to a single low frequency $\kappa_s \sim 12$.

On the bottom panel, we present four periodic orbit families associated with the Trojan orbits and their corresponding single-peaked power spectra in the sample graph below. From left to right, we present the fast Trojan family, the slow Trojan family, the inner galactic circular family, and the outer galactic circular family. In the left two figures, we see that all fast periodic Trojan orbits share a similar frequency and all slow periodic Trojan orbits also share another frequency, both with a small spread. We then mark the two periodic frequencies in all plots with shaded semi-transparent blocks, the higher frequency in blue and the lower in red. Back to the upper panel, the fast and slow periodic orbits stay nicely in their corresponding range of frequencies. On the other hand, each QPO in the middle has two frequencies: a high and a low frequency that falls into the frequency range of the fast and slow closed orbits. In the spectrum of the “thickened” fast QPO, the fast frequency is the dominant frequency. The extended QPO shows an opposite combination, where the low frequency dominates the power spectrum, resulting in an overall banana-shaped morphology. Although not presented, the QPOs of the slow Trojan family only show the banana-shaped morphology and the Fourier spectra always show dominance in the slow frequency. We conclude that the QPOs of the Trojan families can be considered as the superposition of fast and slow modes of Trojan periodic orbits, and the morphology depends on the relative significance of the two frequencies. We note that the tiny side peaks around the fundamental fast and slow frequencies in the QPO plots are harmonics between the two frequencies.

We will see later in §3.4 that the slow Trojan family bifurcates (breaks up) into an inner circular and an outer circular family of periodic orbits that also follows the ZVC. When the Jacobi integral becomes smaller than the effective potential at the saddle points L1 and L2, $E_J < \Phi_{\text{eff}, L2}$, the ZVC prohibits communication between the inner and outer galaxy, resulting in circular ZVC borders and the two circular families. In the lower, rightmost two plots of circular orbits, the frequency starts in the range of the slow frequency but moves to higher frequencies as the E_J drops further and the orbits move away from the Trojan families.

Furthermore, the rim of the volcano in Fig. 2 hinders most of the communication between the inner galaxy (inside the rim) and the outer disc (outside the rim). At typical E_J , the only y-symmetric orbits that explore both sides of the rim are the fast and slow Trojan families. Hence, they have the potential to transport inner galactic stars to the outer disc, and vice versa. As the Sun sits on the outside of the rim, if stars with inner Galactic origins can be found in the SNd, they are likely to be transported by Trojan orbits.

3.2 Kinematics of Trojan orbits in the SNd

To associate the Trojan QPOs that pass through the SNd with the observed overdensities, we make mock observations by integrating the QPOs, obtaining their kinematical information when they pass through the SNd, and comparing their the SNd kinematics to real data.

In the model, QPO families with a range of Jacobi integrals can reach the SNd, be observed, and get mapped into the kinematics plot. Fig. 5 shows a few of the most extended QPOs associated with each periodic orbit. The top panel shows the Trojan QPOs in blue and their parent periodic orbit in red. Their kinematics in the solar

neighbourhood are drawn in the middle panel as red dots, on top of the blue kinematics distribution of *Gaia* stars. Due to the finite time (\sim a Hubble time) of integration, these data appear as a set of lines in the L_Z - V_R plot, but they would cover the whole area for an arbitrarily long integration. We observe that over a range of Jacobi integral, when the QPOs reach the SNd, these orbits cover the Hercules structures and show the asymmetric structure in favour of positive V_R .

Among the orbits, the least energetic orbit (with the lowest E_J) is perturbed from a slow periodic orbit. This QPO populates the highest angular momentum substructure Hercules I, and may possibly go even higher in L_Z into the valley. Next to the right, a slightly more energetic orbit, perturbed from a fast periodic orbit populates Hercules II and a part of Hercules III. The next, more energetic orbit preserves the lowest angular momentum and covers part of Hercules III and Hercules IV. On the rightmost panel, a QPO with extremely high E_J shows the morphology of the thickened circle. This orbit, while can still visit the SNd, includes quite extreme kinematics that get it mapped onto the edge of the plot.

When the perturbation is large, the kinematics map shows a region with a boomerang shape that is concave towards the bottom right. This curvature is similar to the observed curvature in the kinematics distribution constructed by the V_R -biased Hercules II, less-biased Hercules III, and a more biased Hercules IV. While the lower E_J orbits cover regions highly populated by observed stellar kinematics, the highest E_J orbit only visits an area in L_Z - V_R with much lower densities. We attribute this to the fact that these orbits are very energetic, and hence less likely to exist. While they are capable of reaching the SNd to get mapped into the kinematics plot, the lack of members prevents them from forming patterns observable in the kinematics histogram.

The bottom panel of Fig. 5 shows the Fourier-transform power spectrum of the corresponding QPOs. The QPO perturbed from the slow, banana-shaped periodic orbit has the majority of its power in lower frequency, with very little power in the fast frequency. The principal frequency of this QPO with the slow parent orbits is always the slow family. By perturbing the fast family, the parent periodic orbit first “thickens” and then forms the extended morphology. The fast family with the lowest E_J holds QPOs with the thickened morphology that transforms into the extended morphology easily under larger perturbations. With the increase of E_J , the thickened morphology become more stable relative to the extended morphology. While the extended morphology can survive under large perturbations, they are close to the limit of stability and breaks into inner disc circular families further away.

We also investigate how the SNd kinematics vary in the initial condition space (y_0, E_J). In Fig. 6, we hold E_J constant and vary the initial position y_0 in the range of the SNd reaching orbits. For each E_J , we plot the morphology of three QPOs on the left, differentiated by different colours. Then, their the SNd L_Z - V_R kinematics are plotted on the right, labelled by the difference in y_0 to the parent periodic orbit $\Delta y_0 = y_{0,\text{QPO}} - y_{0,\text{PO}}$. The parent periodic orbit of each QPO is presented in black.

The top plot corresponds to the E_J value of a slow family while the middle and bottom plots correspond to two fast families. The figures show that the QPOs cover larger spaces and higher L_Z when perturbed further away from the periodic orbit. The higher E_J orbit can hold QPOs with larger perturbations and cover a wider space. Starting from the closest orbit in magenta, the QPO is mapped to a small egg at first, then distorts towards a boomerang. Larger perturbation increases the distortion of the shape of the region, resulting in larger boomerangs. Moreover, QPOs with lower E_J move further

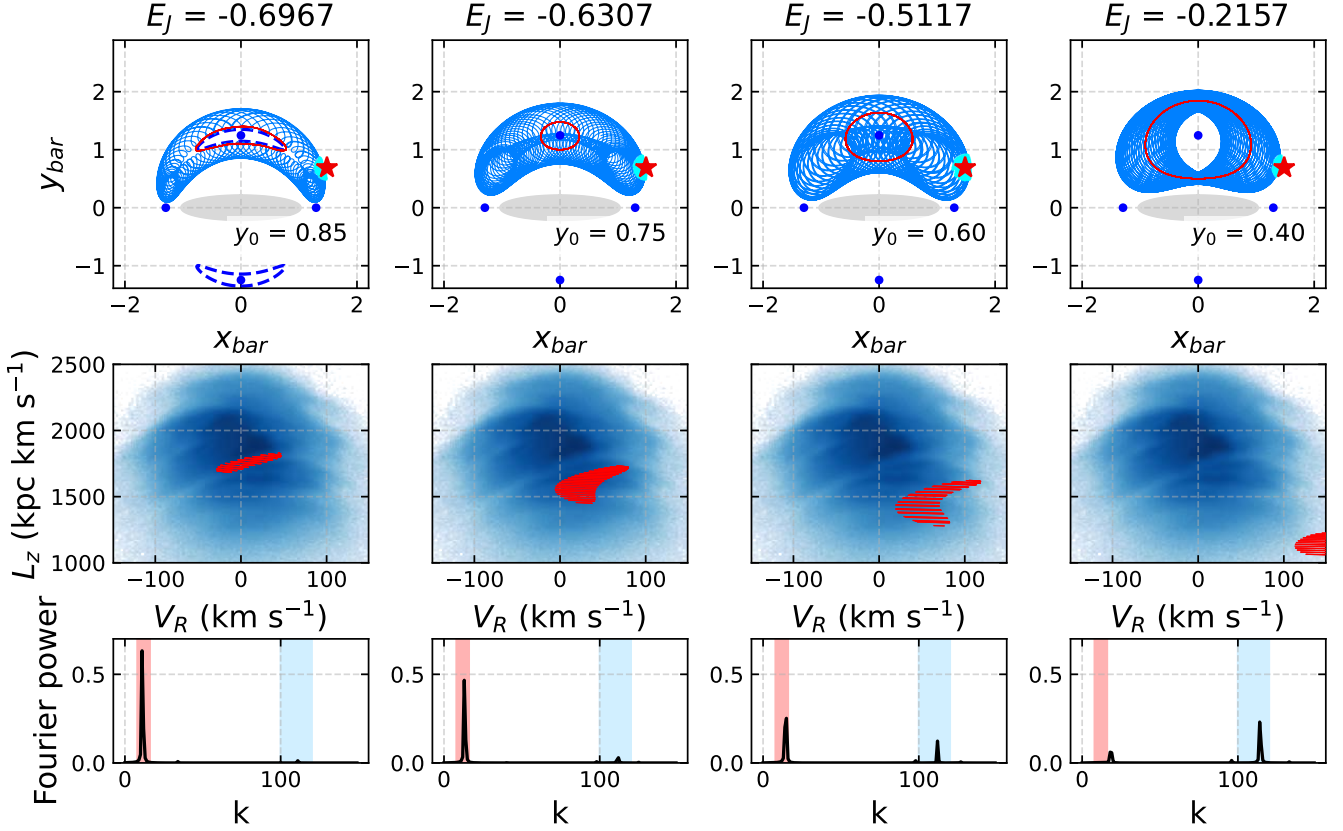


Figure 5. QPOs in the model mapped to the kinematics plane by observation. Top row: the morphology of QPOs is coloured in blue, with the corresponding parent periodic orbit coloured in red. The sun is marked as a red asterisk and the orbits passed through the SNd are coloured cyan; Middle row: the L_Z - V_R kinematics of the corresponding orbit when they pass the SNd. The kinematics are coloured in red on top of the blue *Gaia* kinematics distribution; Bottom row: the Fourier power spectrum of the QPO in the same column. The shaded red and blue blocks mark the frequencies of two periodic Trojan families.

up in L_Z as the perturbation increases, while QPOs with higher E_J are shifted left in V_R . In the presented figures, the QPOs with the lowest E_J cover both Hercules I and II, and the higher E_J orbits cover Hercules II, III, and a portion of Hercules IV.

We note that, at the lowest E_J , slow family QPOs have such high L_Z that their the SNd kinematics go over the valley and join the top fraction of the plot. Several potential explanations can be considered. As noted in § 2.2, our model has a rotation curve slightly higher than the observed Galactic rotation curve. This may result in a systematically higher L_Z in orbits. Another option is to allow Hercules orbits to enter part of the Hyades group. While we observe the existence of a “valley” marked by the non-smooth outskirts between two fractions, a significant fraction of stars still exist around $|V_R| \sim 0$. In this scenario, the more V_R narrowed low E_J QPOs naturally shrink the extended V_R coverage in Hercules III and II. Indeed, some orbits with initial conditions close to Hercules Trojans are found to preserve L_Z - V_R kinematics in agreement with the Hyades group. Other orbits with LSR and Arch/hat kinematics are also observed. These orbits may be potential candidates to help explain the origin of other kinematic groups (see § 4).

Overall, we conclude that, among QPOs observed in the SNd, orbits with higher E_J tend to preserve lower L_Z . QPOs further away from their parent periodic orbits include kinematics with higher L_Z and cover more distorted regions. The lower E_J Trojan QPOs cover Hercules structures with higher L_Z and the higher E_J Trojan QPOs contribute more towards the lower L_Z Hercules subgroups. We note

that these results are sensitive to bar parameters, especially the pattern speed Ω_b . However, the current model $\Omega_b \sim 40 \text{ km s}^{-1} \text{ kpc}^{-1}$ is strongly supported (Portail et al. 2017; Sormani et al. 2015; Monari et al. 2019; Drimmel et al. 2023; Leung et al. 2023).

3.3 Surfaces of section

To understand the mechanism, i.e. the relation between the QPOs and periodic orbits, and the stability of orbits in our model better, the Poincaré surfaces of section are generated for two E_J s, one hosting a fast periodic Trojan orbit, the other hosting a slow rotating Trojan periodic orbit. In a 2-dimensional planar system, the information of orbits is fully embodied in the four-dimensional phase space (x, y, \dot{x}, \dot{y}) . By using the conservation of E_J , the dimension can be reduced to 3D without loss of information. Then by taking a slice through the plane of symmetry, orbits can be distinguished by the topology in the plane, as a reflection of features in the phase space (Hénon & Heiles 1964; Binney et al. 1985).

Chaotic orbits, due to their freedom to explore a higher dimensional region of phase space, cover a 2D area in the surface of section when integrated infinitely. Often, regions explored by chaotic orbits overlap with other chaotic orbits and show no definite pattern on the surface. Periodic orbits, on the other hand, form closed loops in phase space with one or higher multiplicity, and hence, when cut by a plane, they appear as single or a finite set of 0D points. Around loops of stable periodic orbits, the quasiperiodic orbits are confined to, yet

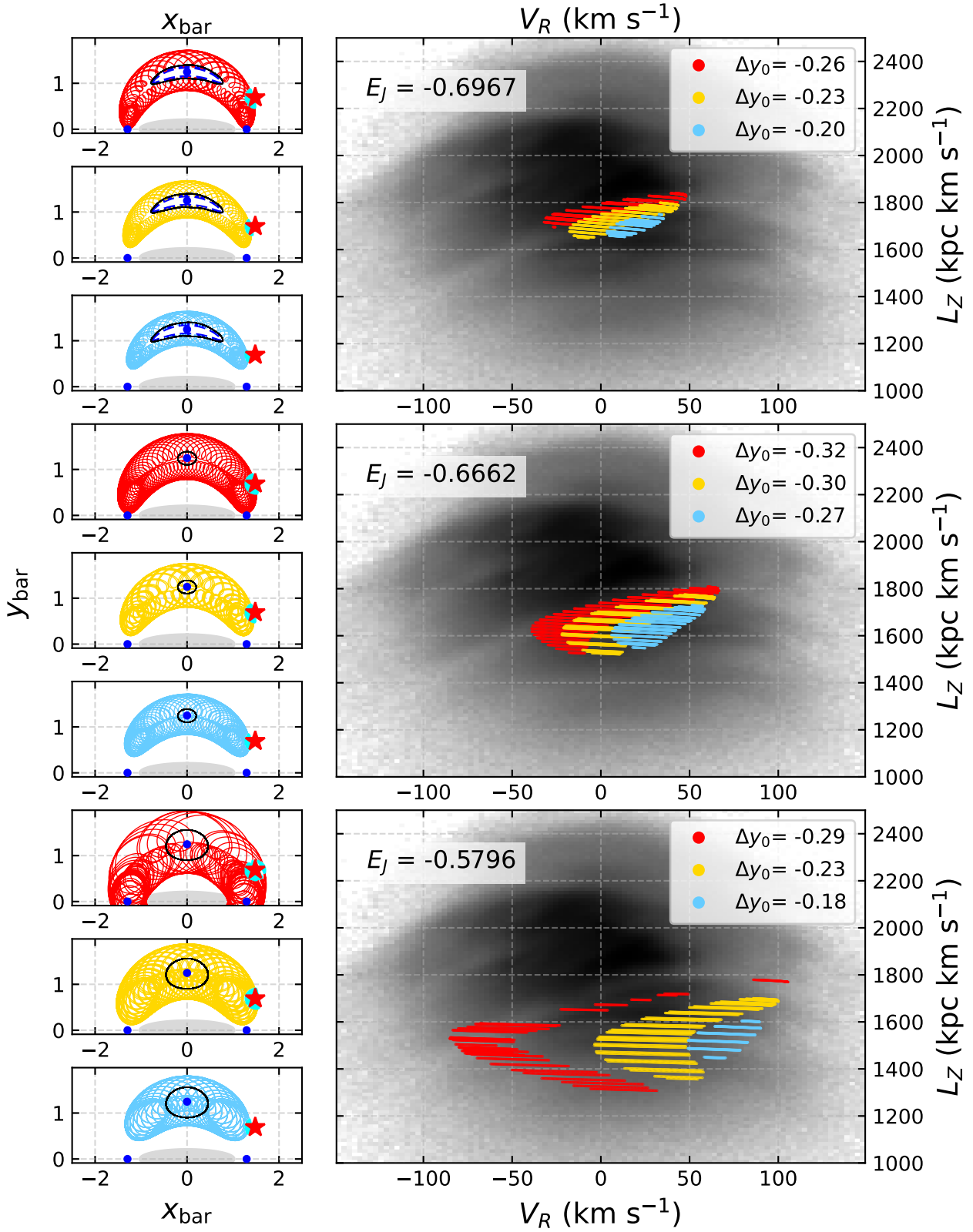


Figure 6. The variation of mock observations of QPOs in the kinematics space with Δy_0 . The kinematics of QPOs in the SNd with three different values for E_J s are presented on the right. For each E_J , three QPOs with different perturbations are presented. The morphologies of the corresponding orbits are plotted on the left in the corresponding colour. From bottom to top in each panel, the perturbation increases from the edge of reaching the SNd to the edge of breaking.

free to explore the surface of the doughnut-shaped tori surrounding the parent periodic orbits. Hence, these orbits appear as one or a set of closed, sometimes very elongated and twisted, 1D curves centred at points representing their parent orbits, the invariant curves. The extent of perturbation the child QPOs can sustain before evolving into chaos or another family works as a measure of the stability of the periodic orbit.

In this study, the surfaces of section of symmetric orbits are generated by cutting through $\dot{y} = 0$ while ensuring $\dot{x} > 0$ at a constant Jacobi Integral E_J . This generates a surface of section on the plane (x, y) . Other works (e.g. Athanassoula et al. 1983; Sellwood & Wilkinson 1993; Cincotta & Simó 2000) often generate surfaces of section in a position-velocity plane, e.g. (y, \dot{y}) or (y, p_y) . The choice of the surface is arbitrary and does not affect the conclusions. Our choice facilitates the relation between spatial features of the orbit and the phase space features on the surface of section.

3.3.1 Surface of section in $E_J = -0.6662$

First, we present the surface of section of a $E_J > \Phi_{\text{eff}, L4}$ which hosts a fast Trojan family. We generate a surface of section plot of $E_J = -0.6662$ with equally spaced initial positions from $y_0 = -2.5$ to $y_0 = 2.5$ with steps of 0.05. The plot of the surface of section is present in the middle of Fig. 7. The morphology of periodic orbits in the (x, y) plane is shown in subplots **a** to **h**. In each morphology plot, a quasi-periodic orbit is plotted in blue under their respective parent periodic orbit. The points in the surface of section plot that correspond to the periodic orbits of each subplot are drawn in the same colour and labelled. As in previous figures, the position of the sun, the Lagrange points, and the bar are marked respectively. Paths of the QPOs are coloured yellow while passing through the solar neighbourhood.

- At the top left, with the highest y_0 , in Fig. 7a, we see an outer disc orbit that turns twice at the bar minor axis outside the L4 and L5 Lagrange points. This is the -2:1 resonance orbit, which is associated with the OLR (Asano et al. 2020). This orbit has two turning circles on the bar minor axis towards the galactic centre and, in the surface of section, is responsible for the three-point structure at about $(x_s, y_s) = (0, 1.4)$ and $(\pm 0.8, -2.2)$, symmetric about the y-axis in the surface of section. Orbits like this are believed to be responsible for the Hercules structure in the fast bar scenario but are beyond the solar neighbourhood in this slow bar model.

- The series of concentric banana shapes centred at $(0, 1.1)$ in the surface of section corresponding to the fast rotating Trojan periodic orbit in Fig. 7b. When perturbed up and down, thickened and extended QPOs form and appear as the thin-elliptical and banana-shaped invariant curves surrounding the point representing the periodic orbit on the surface of section. Before breaking into chaotic orbits, the Trojan family forms a -7:1 island periodic orbit. As seen in subplot 7b, this orbit shows seven turning circles towards the L4 point, in a similar sense to outer galactic resonance orbits towards the galactic centre. These orbits form when two frequencies in the quasi-periodic orbit form a rational ratio.

- Towards the inner galaxy, a 6-turn inner disc hexagonal orbit is found in Fig. 7c. While the specific periodic orbit is generated at $y_0 < 0$, its QPOs are also found around $(0, 0.6)$, below the L4 Trojans in the surface of section. This orbit shows the morphology of a hexagon with turning circles away from the galactic centre. In the surface of section, it is responsible for the five-point structure surrounding the inner galactic disc, at $(0, -1.2)$, $(\pm 1, -0.6)$, and

$(\pm 0.9, 0.3)$. This family explores two sides of the inner galaxy and is less stable.

- Further down, the family breaks into irregular inner galactic chaotic orbits. As seen in the surface of section, this chaotic region covers most of the inner galactic phase space except for three regular regions. Among the three, the only orbit family with a positive y_0 is the rectangular orbits in Fig. 7d. This is a 4-turn family that follows the exterior of the galactic bar. This family forms the three-point structure at $(0, 0.4)$ and $(\pm 0.8, -0.7)$ in the surface of section. This orbit belongs to the x1 orbit family that is believed to be the building block of the galactic bar (Athanassoula et al. 1983, 2009). Unlike the Trojan family, the QPOs of the rectangular family do not change in morphology and only have thickened QPOs. The family breaks into chaos further in.

- Into the centre of the galaxy in the surface of section plot, we find another 4-turn family that has the morphology of a butterfly in Fig. 7e. This orbit also induces a three-point structure in the surface of section at $(0, 0.1)$ and $(\pm 0.5, -0.7)$. We note that the stability of this orbit family can be affected by the existence of the central supermassive black hole and its nuclear stellar disc, so the periodic orbit may not appear in more complicated models like Hunter et al. (2024).

- In Fig. 7f, we see a very stable and extended circular family at $(0, -0.4)$, retrograde in the rotating frame. This orbit has a very high frequency. The QPOs of this family thicken the circle by the typical rosette shape, as the superposition of two frequencies. This family is the most stable and important orbit family in the inner galaxy. As we see in Appendix B, this family exist throughout all E_J s explored and has dominated the phase space as E_J increases.

- Below the L5 Lagrange point, we find the Trojan family on the other side of the galaxy in Fig. 7g. Due to the symmetry of the effective potential along the bar major and minor axes, this family shares the same morphological features as the L4 Trojan family. By further perturbing the orbit to the bottom, we find a circular QPO that explores both sides of the outer disc plane. While we do not find a parent periodic orbit associated, this orbit may be associated with other high L_Z kinematic groups like the Hyades group.

- The periodic orbit with the lowest E_J is found in Fig. 7h. It is a 4-turn outer disc orbit that shows a -4:1 resonance. It appears as the five-point structure at $(0, -2.15)$, $(\pm 1.2, -1.1)$, and $(\pm 1, 0.7)$. This family has QPOs in similar morphology to that of the -2:1 family, and some have argued a possible scenario in which these orbits would contribute to the Hercules structure (Hunt & Bovy 2018; Asano et al. 2020).

3.3.2 Surface of section in $E_J = -0.7193$

In this section, we present the surface of section with an E_J that includes a slow Trojan family. We investigate the impact of lower energy and the existence of ZVC on the phase space of orbits. In Fig. 8, the surface of section plot of $E_J = -0.7193$ is generated in the middle panel with periodic orbits and their corresponding QPOs on the sides, in a similar way to that in § 3.3.1.

- Above the ZVC, we find a very large -1:1 resonance orbit in Fig. 8a. Different from the -2:1 orbit in Fig. 7a, this orbit only turns once above the L4 Lagrange point. Unlike most orbits on the high E_J surface, this orbit does not show symmetry about the bar's major axis. In the surface of section, it corresponds to the point at $(0, 1.6)$ and $(0, -4)$, which is outside the presented surface.

- In Fig. 8b, we present the banana-shaped slow Trojan orbit with the -7:1 island orbit around it. On the surface of section plot, it

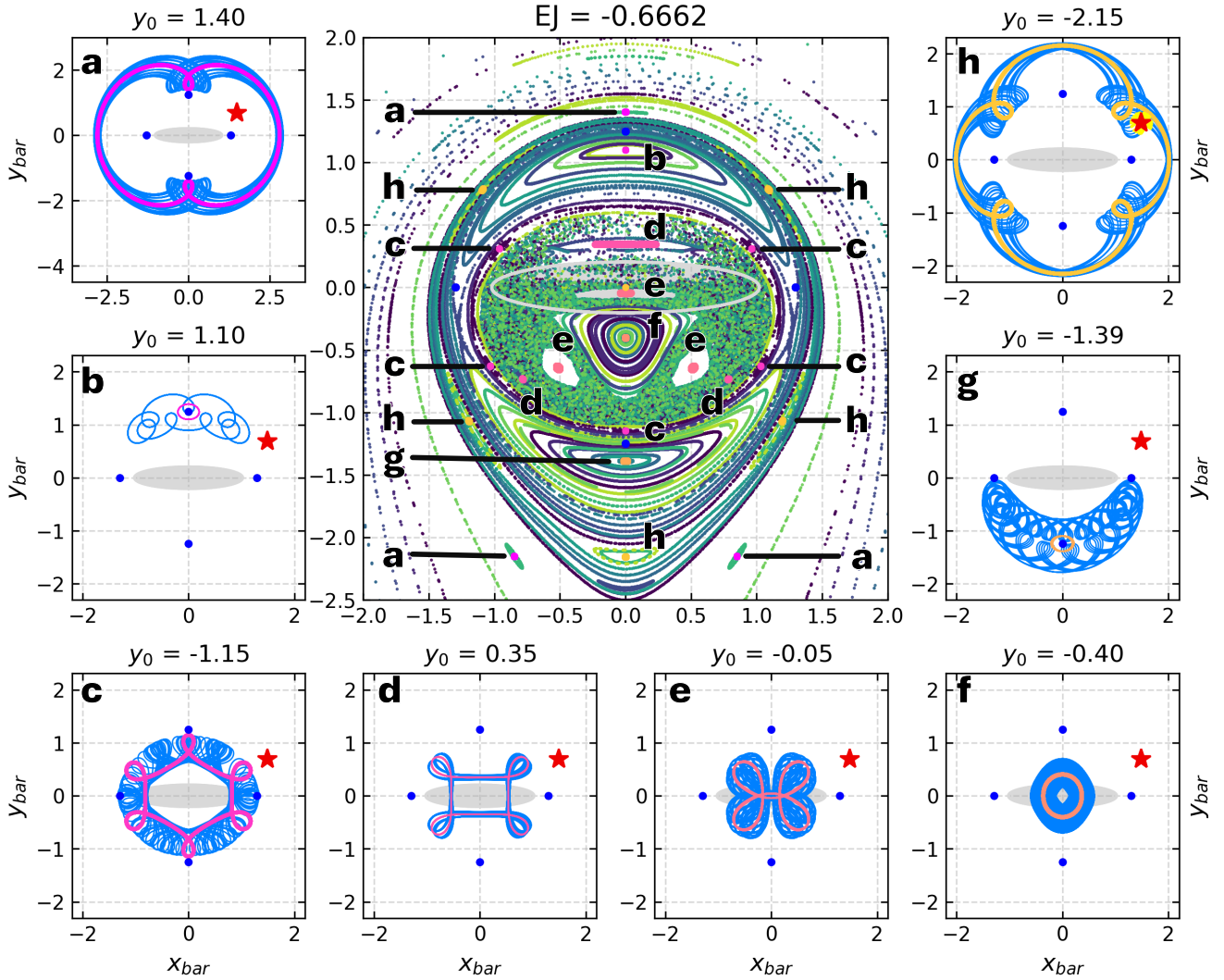


Figure 7. The x - y surface of section and the morphologies of symmetric periodic orbits at $E_J = -0.6662$. In each morphology plot on the side a to h, the periodic orbit is plotted in a warm colour on top of a blue QPO. The sun is marked as a red asterisk and the orbits passed through the SNP are highlighted in yellow. The corresponding points are marked in the same colour and with the label of the plot on the surface of section in the main panel. The bar and Lagrange points are marked the same as the previous plots.

appears as three points at $(0, 1)$ and $(\pm 1.3, 0.4)$, in the middle and two edge points of the ZVC. The island orbit at this energy shows much smaller turning circles than that at the higher E_J .

- Further below, the family of bar surrounding orbits stabilises and shows a 7-turn, 7:1 resonance orbit at the place where the hexagonal orbit is located in Fig. 7. While with a different multiplicity, it also shows a five-point structure in the surface of section at $(0, 0.8)$, $(\pm 1, -0.6)$, and $(\pm 1.2, 0.1)$. Similar to the 7-turn island orbit in subplot b, the turning circles are also significantly smaller than that in the hexagonal orbit.

- In Fig. 8d we encounter again the rectangular family. This rectangular orbit is located at $(0, 0.4)$, and $(\pm 0.8, -0.7)$ in the main panel. The quasi-periodic orbits of this family cover a larger area of the surface of section, showing an increase in significance and stability in the phase space. The turning circles of this orbit also shrink.

- The butterfly orbits in the galactic centre and the inner galactic circular orbits undergo very little morphology transition, except with

smaller turning circles and size. The butterfly orbit in subplot 8e is mapped to $(0, 0)$ and $(\pm 0.5, -0.6)$ in the surface of section, and the circular orbit in 8f is located at $(0, -0.4)$. The two inner galactic orbit families both shrink in the surface of section coverage space as they are limited more by the surface of section.

- On the other side of the ZVC, the L5 slow Trojan orbit is found symmetrical to the L4 family and is mapped onto the surface of section at $(0, -1.5)$. The likely Hyades-related circular QPO is also found by further perturbing the slow Trojans. However, unlike the QPO in § 3.3.1, although with a different morphology, this QPO is found to be a child of the slow Trojan family. See § 4 for a more detailed idea.

- Further below, we arrive at the -4:1 resonance orbit that corresponds to the five-point structure at $(0, -2)$, $(\pm 1.3, -1)$, and $(\pm 1.2, 0.9)$ in the main panel. While morphologically analogous to that in § 3.3.1, the size of turning circles is also reduced.

In general, most orbit families in § 3.3.1 continue to lower E_J . All turning circles of resonance orbits show a size reduction regardless

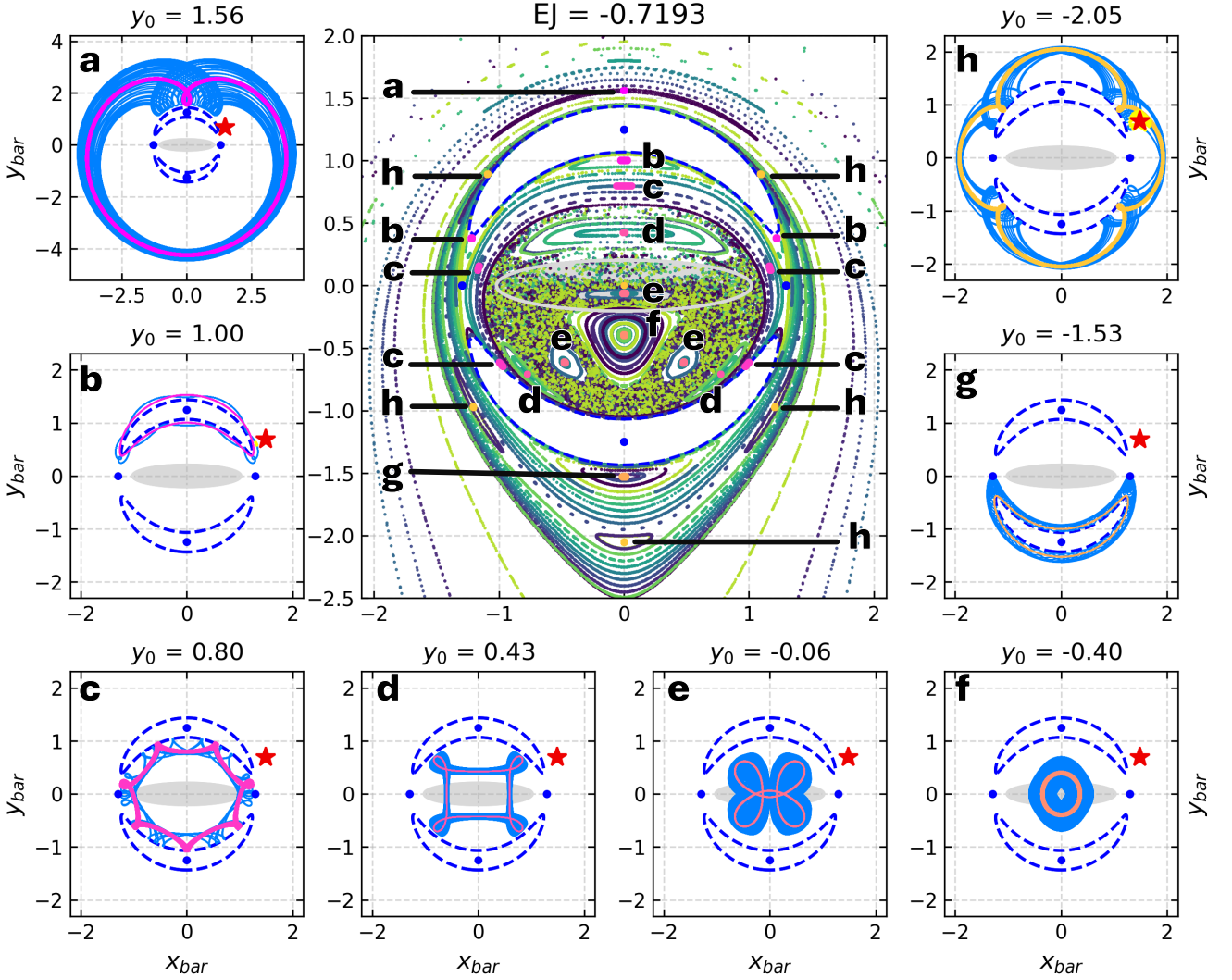


Figure 8. The x - y surface of section and the morphologies of symmetric periodic orbits at $E_J = -0.7193$. Same as Fig. 3.3.1 except with a different E_J .

of whether they are directed toward the galactic centre, away from it, or toward a Lagrange point (as in the case of the $-7:1$ Trojan island). The size of the turning circles is expected to continue to decrease as the E_J goes down, which ultimately results in a change in orbit morphology or encounters a change in the morphology of the phase space. Some $n : 1$ orbits go through morphological changes in the multiplicity of the resonance with the shift in E_J . Along with the coverage of their quasi-periodic orbits, this indicates a lack of stability in these orbit families. Some additional materials on orbits and the evolution of surface of section over E_J can be found in Appendix B. Overall, surface of section plots in Appendix B emphasises the Trojan family and the inner galactic retrograde circular family as the most stable orbit families throughout E_J in addition to the ordinary circular disc families.

Back to the Trojan theory, the fast Trojan family covers a significant portion of the surface of section. While more restricted by the banana-shaped ZVCs, the slow Trojan family also covers a space with a decent amount of surrounding QPOs. These behaviours indicate the strong stability of the Trojan family and the high significance in the phase space. Therefore, we can expect a significant amount of stars to be trapped in this Trojan family. With a high distribution of the stars in

the stable Trojan orbits, it can construct the over-density identified as the Hercules group in Fig. 1.

3.4 Trojan families in the initial condition space

In addition to recognising the importance of Trojan orbits in the phase space with the method of surface of section, it is also curious to learn the stability of the periodic Trojan orbits in the (E_J, y_0) initial condition space.

In Fig. 9, we plot samples of the two Trojan families of periodic orbits and two related families in initial condition space. The Φ_{eff} of the Lagrange points are marked by dashed lines. Among the four-orbit families, the fast Trojan family dominates the initial condition space. Stable fast Trojan periodic orbits are found for $-0.686 < E_J < 0.355$. The fast family become unstable and breaks up at $0.355 < E_J$. Note that for each E_J , two fast Trojan periodic orbits are found, the top with positive y_0 around the L4 and the bottom with negative y_0 around L5. At the magenta line, we have $E_J = \Phi_{\text{eff}, L4}$ and the near-circular fast Trojan orbit reduces to a stationary particle at L4/L5. This is Corotation.

To the left of the magenta line, the Jacobi integral is below the

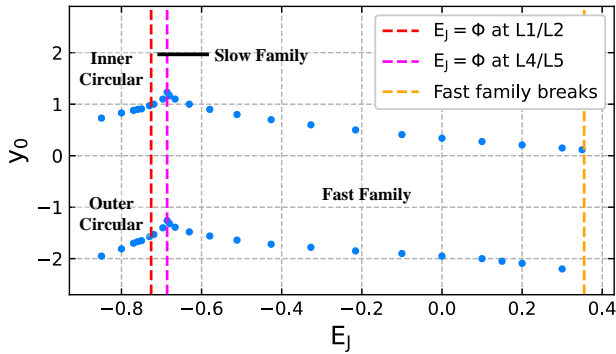


Figure 9. The (E_J, y_0) initial condition space of the Trojan and related periodic orbits. E_J is the conserved Jacobi integral and y_0 is where the orbit crosses the y -axis with $\dot{y} = 0$ and $\dot{x} > 0$. The blue points mark samples of periodic orbits. The vertical dashed orange line marks the maximum E_J that allows the existence of stable fast Trojan periodic orbits. The dashed magenta line marks the $E_J = \Phi_{\text{eff}}$ of the L4 and L5 Lagrange points. The dashed red line marks the $E_J = \Phi_{\text{eff}}$ of the L1 and L2 Lagrange points. The fast family transitions into the slow family between the red and magenta lines. The slow family breaks up into an inner galactic circular family and an outer galactic circular family left to the red line.

maximum effective potential at L4/L5. Thus, ZVC occurs and the fast Trojan orbits transition into a family of slower orbits following the boundaries of the ZVC. Between the red and magenta line, $\Phi_{\text{eff}, L1} < E_J < \Phi_{\text{eff}, L4}$, we observe a small range of $-0.726 < E_J < -0.686$ where the ZVC shows a banana-shaped morphology. With the E_J in this range, particles are not allowed to overcome the potential of the maxima points L4 and L5, but can still find paths through the saddle points L1 and L2 to communicate between the inner and outer disc. By following the ZVC boundaries, the particles form the slow Trojan family and show a similar banana-shaped morphology.

At lower energy, to the left of the red line, the E_J is lower than the effective potential of saddle points L1 and L2. With $E_J < -0.726$, the banana-shaped ZVCs at both sides of the galaxy join at L1 and L2. The new ZVC forbids communication between inner and outer disks and forms two near-circular boundaries. Then, the L4 slow Trojan orbit is encircled by the inner boundary and evolves into an inner disc circular family, prograde in the rotation frame, while the L5 orbit lies outside the outer boundary and evolves into a retrograde outer disc circular family. The morphologies of the two families are shown in the bottom right panels of Fig. 4. As the outer family is less impacted by the asymmetry of the bar, it is expected to be similar to the classical circular orbits in axisymmetric models while the inner family is still affected by the asymmetry induced by the bar. The two families become two of the most stable and significant families in lower energies as seen in Appendix B.

4 DISCUSSION

In Paper I, we discovered a chemically distinct stellar population in Hercules III and IV. These stars are likely to originate from the outer Galactic bar. In our QPO Trojan orbit scenario, these stars can be born on or get caught by the L4 Trojan quasi-periodic orbits which take them through the solar neighbourhood. As more energetic QPOs with higher E_J can cover a larger range of radius in the disc and include lower angular momentum while passing through the SNd, a larger portion of low L_Z Hercules subgroup stars is likely to be formed in

the inner Galaxy, get carried out to the SNd by the high E_J Trojan orbits, and result in a patch of more enhanced [Fe/H] with low L_Z at Hercules III and IV. On the other hand, as Hercules subgroups with higher L_Z are more likely to have lower E_J , which corresponds to less radially extended QPOs, Hercules I and II are more LSR-like in chemical abundances.

Moreover, considering that the sun is located slightly outside the rim of the potential volcano in Fig. 2, transporting stars out from the inner Galaxy requires the underlying mechanism to be capable of overcoming the potential rim. As seen in § 3.3, most stellar orbits in the galactic plane are limited by the potential rim and stay either inside or outside the rim at the presented E_J s. The fast and slow L4 Trojan orbits appear to be the only orbits at these E_J that can cross the rim and thus be capable of transporting inner Galactic stars out. At lower E_J , as discussed in § 3.4, the ZVC prohibits the communication between the inner and outer disc, and hence no orbit can cross the rim. At higher E_J , the turning circles expand with the increase of E_J and can result in rim-crossing orbits. However, they generally do not include the right kinematics of Hercules and are more likely to contribute to the background. In addition, higher E_J requires higher energy, resulting in a lower probability: while these orbits are stable and capable of transporting, they are less likely to exist in the disc.

Furthermore, the surfaces of section in Appendix B reveals the Trojan families, especially the fast family, as the second-most stable family throughout E_J . The most stable family is the retrograde inner galactic circular orbit shown in Fig. 7. These orbits are inner galactic orbits that cannot visit the SNd even at extremely high $E_J \sim 0$. Therefore, considering the stability and the capability to transport inner disc stars out, the Trojan orbits are the most likely orbits that could be responsible for the Hercules group in the SNd.

Apart from the inner disc stars born on the Trojan orbits, we are curious about how stars in the inner disc can be captured into the Trojan orbits and move outwards to the SNd. When the stars are close to the bar, the asymmetry of the bar potential defines the Jacobi integral $E_J = E - \Omega_b \cdot L_Z$ as the only general integral of motion. Therefore, unlike symmetric disc stars that have the conservation of energy and stay at a point in the (L_Z, E) plane, bar-related orbits move on the straight line with a constant gradient of Ω_b and different offsets defined by the constant E_J . Then, if an unstable orbit approaches a Trojan orbit that happens to be on the same line in the (L_Z, E) plane, it may be captured into the more stable Trojan orbit. Consider that the chemical abundances suggest a Hercules origin close to the super-thin-outer-bar, while the exact mechanism supporting the super-thin-bar is not yet well understood, its thickness creates a plausible scenario in which orbits that are unstable under vertical perturbations support the unusually thin structure. Then, if an unstable super-thin-bar orbit can be found fulfilling the previous conditions, it may be captured by a Trojan orbit and escape the potential of the bar. Another region close to the outer bar is the L1 and L2 Lagrange points. As unstable critical points, while orbits around there are unstable in nature, if certain orbits or gas can be trapped around, the instability should allow them to be captured easily by other orbits, including the Trojans.

To consider these questions, we need a less general, more realistic, and more complicated self-consistent model of the Galaxy to consider orbits in the inner Galaxy and the origin of the super thin bar. We plan to investigate these issues in the future. We plan to adopt a more realistic, observation-based, 3D potential of the Milky Way that includes details of the inner Galaxy with a boxy peanut-shaped bulge and a super thin long bar (Sormani et al. 2022; Hunter et al. 2024). We will use this more accurate model to consider possible

inner galactic orbits that might be captured by the Trojan orbits and the origins of the super thin bar that has a vertical scale height of only 40 pc (Wegg et al. 2015).

Another natural extension of this study is to extend the influence of orbits in this barred model to other kinematic structures in the SNd. In Fig. 10, we present a few orbits that may potentially contribute to explaining the other the SNd structures. In this figure, each row corresponds to an orbit: the morphology of the orbit is shown in the left; the the SNd L_Z - V_R kinematics is presented in the middle; and their corresponding surface of section is plotted on the right to identify the orbit families they belong to. From the top, the first row shows a QPO of the outer circular orbit discussed in § 3.4. At this radius, the non-axisymmetric influence of the bar is very small so the orbit lives in a nearly axisymmetric environment. This orbit includes the SNd kinematics in the Arch/Hat. These orbits can bring disc stars from a larger radius to the SNd. These outer disc stars are expected to be more Fe-deficient. In Paper I, the Hat was found with consistent chemical information to these orbits.

In the second row, we present a circular QPO that includes the SNd kinematics of the peak of Hyades group. The surface of section plot indicates it as a QPO of the slow Trojan family. Further below, another peculiar circular QPO is found without a parent periodic orbit. This orbit also includes the kinematics of the Hyades group in SNd, but unlike the previous orbit, it has a much larger dispersion in V_R . Considering the structures in the L_Z - V_R kinematic space, the two families of orbits can both contribute to the Hyades group in SNd.

The bottom row shows a fast Trojan orbit responsible for the Hercules group we discussed extensively in this paper. A few QPOs of the -4:1 resonant orbit also include L_Z similar to Hyades but with a much larger dispersion in V_R . This can potentially be related to the origin of the valley between the high L_Z groups and Hercules. Orbits in the barred dynamics model may potentially be a uniform mechanism that explains most of the major kinematic structures in the SNd. If this is correct, it could be possible to find a distribution in the (y_0, E_J) initial condition space whose orbits recreate the distribution of the L_Z - V_R kinematics space in the SNd.

5 CONCLUSIONS

In this paper, we investigated the Trojan scenario of the underlying mechanism of the Hercules group with a barred galaxy model with a long slow bar that reflects our current best understanding of the Galactic bar. By combining our analysis of stellar chemical data from GALAH DR4 and APOGEE DR17 in Paper I, we arrive at the following conclusions:

- Two periodic orbit families are associated with the L4 Lagrange point, at Corotation resonance with the galactic bar. One of the families is a near-circular fast family that cuts through contour lines of the effective potential, while the other is a slow family that follows the banana-shaped contour line around the L4. While both families are not allowed to visit the SNd directly, their stability allows them to form very extended quasi-periodic orbits that can visit the SNd. In the SNd, these QPOs include the L_Z - V_R kinematics of the Hercules group with a favoured bias towards positive V_R .
- By applying tools of surface of section, the Trojan orbits are found highly stable and cover a significant volume in the phase space. Through mock observations, we find that QPOs with higher E_J hold more extended QPOs which include lower L_Z in the SNd. Thus, high L_Z Hercules subgroups are more likely to be associated with low E_J

Trojan QPOs and low L_Z Hercules structures were likely related to high E_J Trojan QPOs.

- The super metal-rich, super odd-Z rich, and slightly more alpha-poor population found in Paper I in the low L_Z Hercules subgroups is expected to have an inner Galactic origin around the outer thin bar. Our orbital analysis suggests that they are likely captured by the high E_J Trojan orbit to visit the SNd and hence include the lowest L_Z in the SNd.

- We reveal that the orbits in our barred model could contribute to explaining other kinematic overdensity structures in SNd. Early results associated circular orbits with LSR kinematics; QPOs of circular orbits from the outer disc with the hat group; and some peculiar circular QPOs related to the Trojan orbit families with the Hyades group.

Our future work will consider a more realistic potential, explore possible origins of the super thin bar, and investigate possible scenarios of the capture of inner Galactic stars into Trojan orbits.

ACKNOWLEDGEMENTS

We acknowledge the traditional owners of the land on which the AAT and ANU stand, the Gamilaraay, the Ngunnawal and Ngambri people. We pay our respects to elders past, present, and emerging and are proud to continue their tradition of surveying the night sky in the Southern hemisphere.

HJ thanks the Queensland University School of Mathematics and Physics for hospitality and funding support as part of their distinguished visitor program.

SOFTWARE

The research for this publication was coded in Python v. 3.12 and included packages Astropy v. 6.0.0 (Astropy Collaboration et al. 2013, 2018, 2022), IPython v. 6.27.1 (Pérez & Granger 2007), Matplotlib v. 3.8.2 (Hunter 2007), NumPy v. 1.26.4 (Harris et al. 2020), SciPy v. 1.11.4 (Virtanen et al. 2020), and tqdm v. 4.66.1 (da Costa-Luis et al. 2024).

DATA AVAILABILITY

The Python code with the Ferrers barred potential is available in <https://github.com/HYuleep/FerrersModel>. Code used for data analysis and plotting are available on request. *Gaia* DR3 (Gaia Collaboration et al. 2023) can be obtained via *Gaia* archive.

REFERENCES

- Abdurro'uf et al., 2022, *ApJS*, 259, 35
 Antoja T., et al., 2014, *A&A*, 563, A60
 Asano T., Fujii M. S., Baba J., Bédorf J., Sellentin E., Portegies Zwart S., 2020, *MNRAS*, 499, 2416
 Asplund M., Grevesse N., Sauval A. J., Scott P., 2009, *ARA&A*, 47, 481
 Astropy Collaboration et al., 2013, *A&A*, 558, A33
 Astropy Collaboration et al., 2018, *AJ*, 156, 123
 Astropy Collaboration et al., 2022, *ApJ*, 935, 167
 Athanassoula E., 1992, *MNRAS*, 259, 328
 Athanassoula E., Bienayme O., Martinet L., Pfenniger D., 1983, *A&A*, 127, 349
 Athanassoula E., Romero-Gómez M., Bosma A., Masdemont J. J., 2009, *MNRAS*, 400, 1706

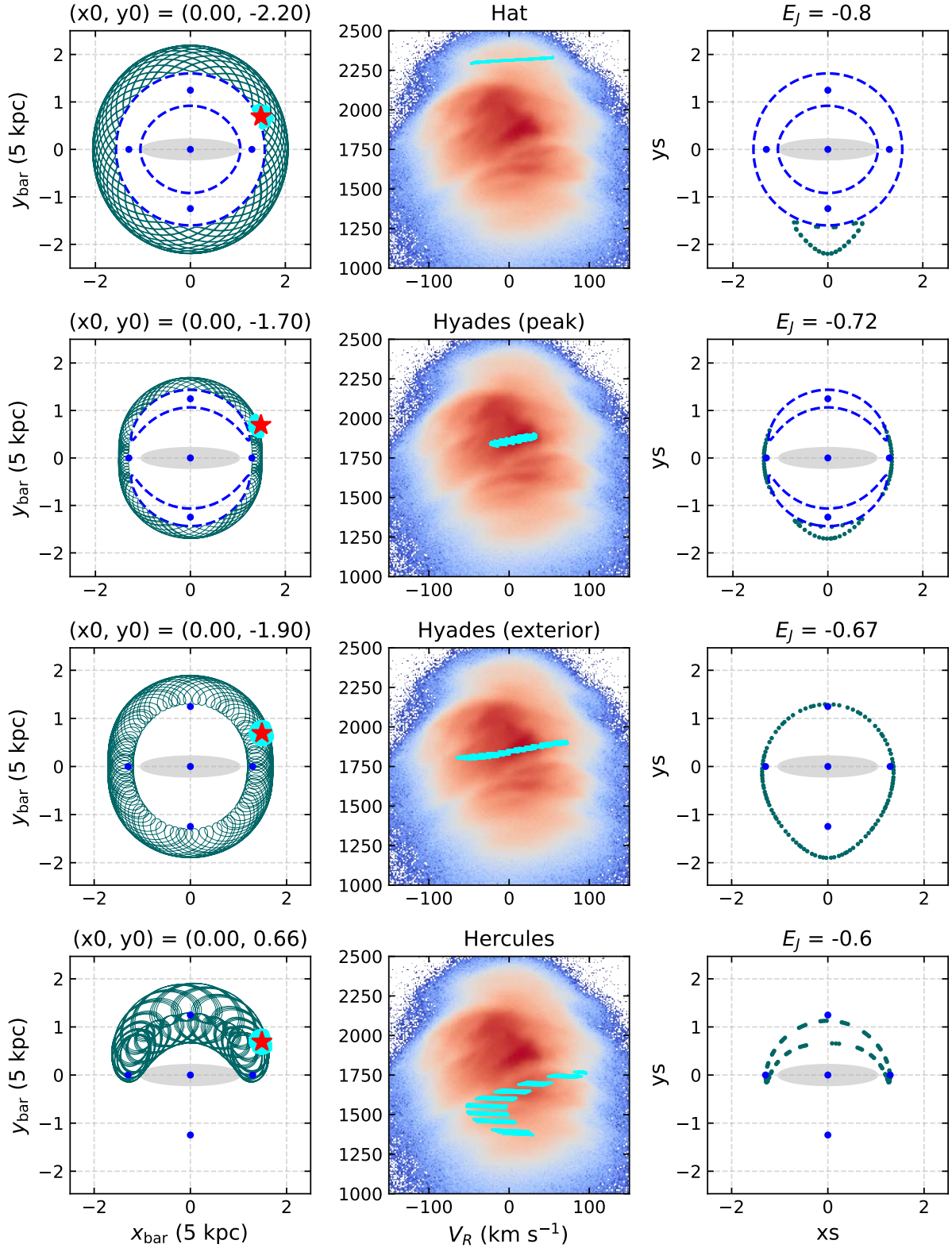


Figure 10. Examples of orbits that can potentially contribute to other kinematic structures. For every row, an orbit is generated on the Galactic plane; the orbit's the SNd kinematics is marked in cyan in the middle; and the surface of section of the orbit is presented on the right. From top to bottom, we present four orbits corresponding to the kinematics of the Hat, Hyades, and Hercules.

Barros D. A., Pérez-Villegas A., Lépine J. R. D., Michtchenko T. A., Vieira R. S. S., 2020, *ApJ*, **888**, 75
 Bensby T., Oey M. S., Feltzing S., Gustafsson B., 2007, *ApJ*, **655**, L89
 Binney J., 2020, *MNRAS*, **495**, 895
 Binney J., Spergel D., 1982, *ApJ*, **252**, 308
 Binney J., Tremaine S., 2008, *Galactic Dynamics: Second Edition*
 Binney J., Gerhard O. E., Hut P., 1985, *MNRAS*, **215**, 59
 Brent R. P., 1973, *Algorithms for Minimization without Derivatives*, 1st edn. Prentice-Hall, Englewood Cliffs, New Jersey
 Buder S., et al., 2024, *arXiv e-prints*, p. [arXiv:2409.19858](https://arxiv.org/abs/2409.19858)
 Cincotta P. M., Simó C., 2000, *A&AS*, **147**, 205
 D’Onghia E., L. Aguerri J. A., 2020, *ApJ*, **890**, 117
 Dehnen W., 2000, *AJ*, **119**, 800
 Drimmel R., et al., 2023, *A&A*, **670**, A10
 Eggen O. J., 1983, *AJ*, **88**, 642
 Eggen O. J., 1996, *AJ*, **112**, 1595
 Eilers A.-C., Hogg D. W., Rix H.-W., Ness M. K., 2019, *ApJ*, **871**, 120
 Famaey B., Jorissen A., Luri X., Mayor M., Udry S., Dejonghe H., Turon C., 2005, *A&A*, **430**, 165
 Ferrers N. M., 1877, *The Quarterly Journal of Pure and Applied Mathematics*, **14**, 1
 Freeman K. C., 1966, *MNRAS*, **133**, 47
 GRAVITY Collaboration et al., 2019, *A&A*, **625**, L10
 GRAVITY Collaboration et al., 2021, *A&A*, **647**, A59
 Gaia Collaboration et al., 2023, *A&A*, **674**, A1
 Harris C. R., et al., 2020, *Nature*, **585**, 357
 Henon M., Heiles C., 1964, *AJ*, **69**, 73
 Hunt J. A. S., Bovy J., 2018, *MNRAS*, **477**, 3945
 Hunt J. A. S., Hong J., Bovy J., Kawata D., Grand R. J. J., 2018, *MNRAS*, **481**, 3794
 Hunter J. D., 2007, *Computing in Science & Engineering*, **9**, 90
 Hunter G. H., et al., 2024, *arXiv e-prints*, p. [arXiv:2403.18000](https://arxiv.org/abs/2403.18000)
 Kalnajs A. J., 1991, in Sundelius B., ed., *Dynamics of Disc Galaxies*. p. 323
 Khoperskov S., Gerhard O., 2022, *A&A*, **663**, A38
 Kim W.-T., Seo W.-Y., Kim Y., 2012, *ApJ*, **758**, 14
 Leung H. W., Bovy J., Mackereth J. T., Hunt J. A. S., Lane R. R., Wilson J. C., 2023, *MNRAS*, **519**, 948
 Liang X., Yoon S.-J., Zhao J., Li Z., Zhang J., Wu Y., 2023, *ApJ*, **956**, 146
 Lucchini S., D’Onghia E., Aguerri J. A. L., 2024, *MNRAS*, **531**, L14
 Michtchenko T. A., Lépine J. R. D., Pérez-Villegas A., Vieira R. S. S., Barros D. A., 2018, *ApJ*, **863**, L37
 Monari G., Kawata D., Hunt J. A. S., Famaey B., 2017, *MNRAS*, **466**, L113
 Monari G., Famaey B., Siebert A., Wegg C., Gerhard O., 2019, *A&A*, **626**, A41
 Murray C. D., Dermott S. F., 1999, *Solar System Dynamics*, [doi:10.1017/CBO9781139174817](https://doi.org/10.1017/CBO9781139174817).
 Pagel B. E. J., Edmunds M. G., 1981, *ARA&A*, **19**, 77
 Perek L., 1962, *Advances in Astronomy and Astrophysics*, **1**, 165
 Pérez F., Granger B. E., 2007, *Computing in Science and Engineering*, **9**, 21
 Pérez-Villegas A., Portail M., Wegg C., Gerhard O., 2017, *ApJ*, **840**, L2
 Portail M., Gerhard O., Wegg C., Ness M., 2017, *MNRAS*, **465**, 1621
 Quillen A. C., et al., 2018, *MNRAS*, **478**, 228
 Sellwood J. A., Wilkinson A., 1993, *Reports on Progress in Physics*, **56**, 173
 Sormani M. C., Binney J., Magorrian J., 2015, *MNRAS*, **454**, 1818
 Sormani M. C., et al., 2022, *MNRAS*, **512**, 1857
 Virtanen P., et al., 2020, *Nature Methods*, **17**, 261
 Wegg C., Gerhard O., Portail M., 2015, *MNRAS*, **450**, 4050
 Wheeler A., Abril-Cabezas I., Trick W. H., Fragkoudi F., Ness M., 2022, *ApJ*, **935**, 28
 Yusen L., Freeman K., Jerjen H., Buder S., Hayden M., Mondal A., 2024, in preparation
 da Costa-Luis C., et al., 2024, tqdm: A fast, Extensible Progress Bar for Python and CLI, [doi:10.5281/zenodo.595120](https://doi.org/10.5281/zenodo.595120)
 de Vaucouleurs G., Freeman K. C., 1972, *Vistas in Astronomy*, **14**, 163

APPENDIX A: THE FERRERS BAR POTENTIAL

This section presents the method used to calculate the Ferrers spheroidal bar potential model.

A1 The potential

The density of the Ferrer’s spheroidal bar is

$$\rho = \rho_0(1 - m^2)^2, \quad \text{where } m(x, y) = \frac{x^2}{a^2} + \frac{y^2}{c^2},$$

for $m \leq 1$, where $a > c$ and $\epsilon^2 = a^2 - c^2$. Define $\psi(x, y)$ by,

$$y^2 \tan^2 \psi + x^2 \sin^2 \psi = \epsilon^2 \quad (m > 1), \quad (\text{A1})$$

$$\cos \psi = \frac{c}{a} \quad (m < 1). \quad (\text{A2})$$

Define

$$W_{lk} = 2 \int_0^\psi \tan^{2l-1} \theta \sin^{2k-1} \theta d\theta. \quad (\text{A3})$$

Write $x = \bar{x}\epsilon$, $y = \bar{y}\epsilon$, $a = \bar{a}\epsilon$, then the potential is

$$\Phi = \frac{\pi G \rho_0 a c^2}{\epsilon} \bar{\Phi},$$

where, by dropping tildes,

$$\begin{aligned} \bar{\Phi} = & \frac{1}{3} W_{10} - (y^2 W_{20} + x^2 W_{11}) + (y^4 W_{30} + 2y^2 x^2 W_{21} + x^4 W_{12}) \\ & - \frac{1}{3} (y^6 W_{40} + 3y^4 x^2 W_{31} + 3y^2 x^4 W_{22} + x^6 W_{13}). \end{aligned}$$

The mass of the bar is $M = 32\pi\rho_0 a c^2 / 105$. Let the bar rotate with angular velocity Ω . Write

$$Q = \frac{105GM}{32\Omega^2 \epsilon^3}.$$

Then

$$\Phi = Q\Omega^2 \epsilon^2 \bar{\Phi}.$$

A2 The potential gradient

Within the bar ($m < 1$), $W+lks$ are constant and the potential gradient is

$$\begin{aligned} \frac{\partial \bar{\Phi}}{\partial x} = & -2xW_{11} + (4xy^2W_{21} + 4x^3W_{12}) \\ & - (2xy^4W_{31} + 4x^3y^2W_{22} + 2x^5W_{13}), \end{aligned}$$

$$\begin{aligned} \frac{\partial \bar{\Phi}}{\partial y} = & -2yW_{20} + (4y^3W_{30} + 4x^2yW_{21}) \\ & - (2y^5W_{40} + 4x^2y^3W_{31} + 2x^4yW_{22}). \end{aligned}$$

Outside the bar ($m > 1$), $W_{lk} = W_{lk}(x, y)$ are functions of x and y . Then,

$$\begin{aligned} \frac{\partial \tilde{\Phi}}{\partial x} = & \frac{1}{3} \frac{\partial W_{10}}{\partial x} - (y^2 \frac{\partial W_{20}}{\partial x} + x W_{11} + x^2 \frac{\partial W_{11}}{\partial x}) \\ & + (y^4 \frac{\partial W_{30}}{\partial x} + 4xy^2 W_{21} + 2x^2 y^2 \frac{\partial W_{21}}{\partial x} + x^4 \frac{\partial W_{12}}{\partial x} + 4x^3 W_{12}) \\ & - \frac{1}{3} (y^6 \frac{\partial W_{40}}{\partial x} + 6xy^4 W_{31} + 3x^2 y^4 \frac{\partial W_{31}}{\partial x} + 3x^4 y^2 \frac{\partial W_{22}}{\partial x} \\ & + 12x^3 y^2 W_{22} + x^6 \frac{\partial W_{13}}{\partial x} + 6x^5 W_{13}) \end{aligned}$$

$$\begin{aligned} \frac{\partial \tilde{\Phi}}{\partial y} = & \frac{1}{3} \frac{\partial W_{10}}{\partial y} - (2y W_{20} + y^2 \frac{\partial W_{20}}{\partial y} + x^2 \frac{\partial W_{11}}{\partial y}) \\ & + (4y^3 W_{30} + y^4 \frac{\partial W_{30}}{\partial y} + 4x^2 y W_{21} + 2x^2 y^2 \frac{\partial W_{21}}{\partial y} + x^4 \frac{\partial W_{12}}{\partial y}) \\ & - \frac{1}{3} (6y^5 W_{40} + y^6 \frac{\partial W_{40}}{\partial y} + 12x^2 y^3 W_{31} + 3x^2 y^4 \frac{\partial W_{31}}{\partial y} \\ & + 6x^4 y W_{22} + 3x^4 y^2 \frac{\partial W_{22}}{\partial y} + x^6 \frac{\partial W_{13}}{\partial y}) \end{aligned}$$

A3 Computing the potential gradient

In equation A3, substitute $u = \sin \theta$; $v(x, y) = \sin \psi$. Then,

$$W_{lk} = 2 \int_0^v \frac{u^{2l+2k-2} du}{(1-u^2)^l}. \quad (\text{A4})$$

From equations A1 and A2,

$$x^2 v^2 (1-v^2) + y^2 v^2 + v^2 = 1 \quad \text{for } m > 1, \quad (\text{A5})$$

$$v = \frac{1}{a} \quad \text{for } m \leq 1. \quad (\text{A6})$$

Equation A5 is an ellipse in (x, y) with semi-axes $(1/v)$ and $\sqrt{(1+v^2)}/v$. For $v = a$, the ellipse is the edge of the Ferrer's bar.

The derivatives of W_{lk} are,

$$\frac{\partial W_{lk}}{\partial x} = 2 \frac{v^{2l+2k-2}}{(1-v^2)^l} \frac{\partial v}{\partial x}, \quad \text{where,}$$

$$\frac{\partial v}{\partial x} = \frac{-xv(1-v^2)}{x^2(1-2v^2) + y^2 + 1},$$

$$\frac{\partial v}{\partial y} = \frac{-yv}{x^2(1-2v^2) + y^2 + 1}.$$

The package `scipy.optimize.brentq` (Brent 1973) is adopted to derive v from equation A5.

A4 Recurrence relations for W

Start from equation A4. Define 6 integrals:

$$J_n = 2 \int \frac{v^{2n} dv}{(1-v^2)^{n+2}} \quad I_n = 2 \int v^{2n} dv,$$

for $n = 0, 1, 2$,

$$J_0 = \frac{1}{2} \left(\frac{2v}{1-v^2} + \log \frac{1+v}{1-v} \right),$$

$$J_1 = \frac{1}{8} \left(\frac{2v(1+v^2)}{(1-v^2)^2} - \log \frac{1+v}{1-v} \right),$$

$$J_2 = \frac{1}{48} \left(\frac{2v(3v^4 + 8v^2 - 3)}{(1-v^2)^3} + \log \frac{1+v}{1-v} \right).$$

We obtain W_{10} and W_{40} directly,

$$W_{10} = \log \frac{1+v}{1-v},$$

$$W_{40} = \frac{66v^4 - 80v^3 - 15(1-v^2)^3 W_{10} + 30v}{48(1-v^2)^3}.$$

Then the remaining terms can be obtained by recurrence relations,

$$W_{20} = J_0 - W_{10},$$

$$W_{30} = J_1 - W_{20},$$

$$W_{40} = J_2 - W_{30},$$

$$W_{11} = W_{10} - I_0,$$

$$W_{12} = W_{11} - I_1,$$

$$W_{13} = W_{12} - I_2,$$

$$W_{21} = W_{20} - W_{11},$$

$$W_{22} = W_{21} - W_{12},$$

$$W_{31} = W_{30} - W_{21}.$$

APPENDIX B: THE EVOLUTION OF SURFACE OF SECTION SPACE

In this section, surfaces of section with E_J from -0.85 to 0.00 . Throughout all E_J , the inner circular retrograde family shown in Figures 7f and 8f is the most stable family. At super high E_J this family expands on the surfaces, showing significant increases in stability. The increased energy and stability also result in the appearance of more island orbits in the family. At E_J below Φ_{L2} , the outer retrograde circular family becomes the dominant family in the outer disc. As seen in Fig. 10, the outer circular family can be associated with the most regular planar circular motions in the disc. Apart from these, the Trojan families, especially the fast Trojan family, cover a large area on the surface, indicating their identity as the next most stable orbit after the previous circular orbits.

This paper has been typeset from a $\text{\TeX}/\text{\LaTeX}$ file prepared by the author.

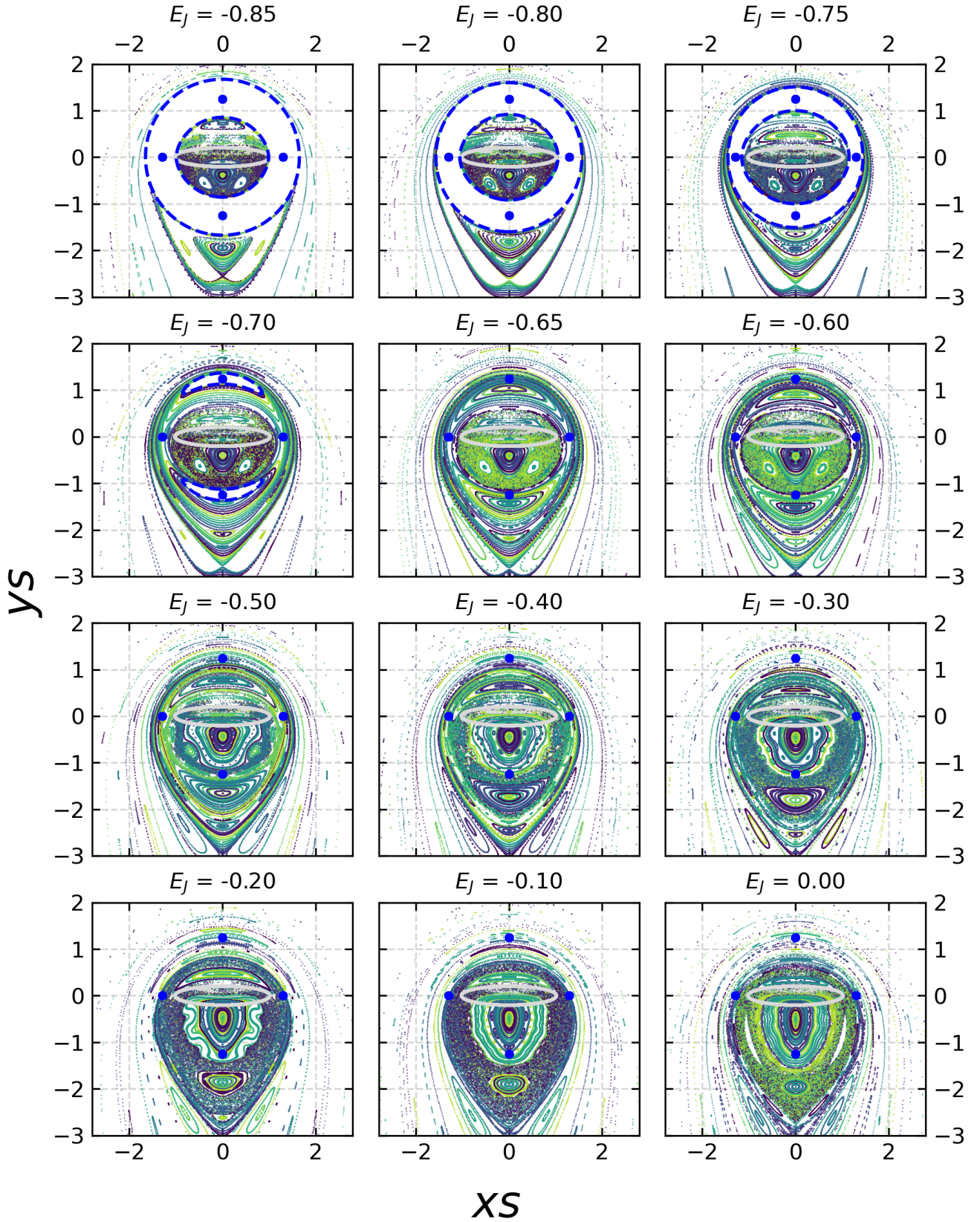


Figure B1. The variation of orbit families on the x - y surface of section over E_J from $E_J = -0.85$ to $E_J = 0.00$. The fast Trojan orbit family covers a large extent in the phase space and exists over a large range of E_J s. The central retrograde circular family is the most stable family that exist across all the E_J presented.